Wave load effect analysis of a floating bridge in a fjord considering inhomogeneous wave conditions

Zhengshun Cheng[a,b,c,*], Zhen Gao[a,b,c], Torgeir Moan[a,b,c]

[a] *Department of Marine Technology, Norwegian University of Science and Technology (NTNU), Trondheim, 7491, Norway*
[b] *Centre for Ships and Ocean Structures (CeSOS), NTNU, Trondheim, 7491, Norway*
[c] *Centre for Autonomous Marine Operations and Systems (AMOS), NTNU, Trondheim, 7491, Norway*

Abstract

When designing a floating bridge crossing a deep and wide fjord, a homogeneous wave field is usually assumed for simplicity. However, waves in fjords are commonly inhomogeneous, and hence the mentioned design practice introduces uncertainty, which should be assessed for the design. In this study, we proposed an approach to account for the inhomogeneous wave load effect on a floating bridge and applied it on a floating bridge that was initially proposed for crossing the Bjørnafjorden. The floating bridge considered is end-anchored, about 4600 m long and consists of a cable-stayed high bridge and a low bridge supported by 19 pontoons. Wave excitation loads on each pontoon were proposed to be modeled and applied separately to account for inhomogeneous waves. By considering 1-year and 100-year wave conditions, dynamic responses of the floating bridge subjected to homogeneous and inhomogeneous waves were analyzed and compared. It is found that inhomogeneous waves cause relatively larger sway motion, axial force, and strong axis bending moment, as well as significantly larger weak axis bending moment along the bridge girder than homogeneous waves. These responses depend on the inhomogeneity level of waves considered. Proper description of the wave field is therefore very important for evaluating the effect of inhomogeneous waves and associated uncertainties.

*Corresponding author. Email address: zhengshun.cheng@ntnu.no

Keywords: floating bridge, fjord, wave load effect, homogeneous wave, inhomogeneous wave

1. Introduction

Floating bridges have a very long history, dated back to 2000 BC [1]. But they have been used as road links in modern infrastructure since around 1940. A worldwide development of floating bridges was summarized by Watanabe [1] and Kvåle [2], including the Hood Canal bridge in the USA [3], the Bergsøysund bridge [4, 5] and the Nordhordland bridge [6] in Norway, and the Yumemai bridge [7] in Japan, etc.

A number of studies have been conducted to investigate the dynamic behavior of floating bridges. Løken et al. [8] conducted the model test of a pontoon type floating bridge in wave basin at MARINTEK (now SINTEF Ocean), and numerical results presented a fairly good agreement with those from the model test. Watanabe et al. [7] reviewed the design of the Yumemai Bridge, a floating swing arch bridge. Many issues related to the design were addressed, including the action of waves, wind and earthquakes, the required swinging mechanism and the issue of durability. Kvåle et al. [4] developed a frequency domain method to account for the hydroelastic responses of pontoon type floating bridges, and applied it to investigate the dynamic behavior of the Bergsøysund bridge. Based on field measurement data, Kvåle et al. [5] carried out an operational modal analysis for the Bergsøysund bridge. Raftoyiannis [9] presented a simple approach for studying the dynamic response of floating bridges due to moving loads and traveling waves. Petersen and Øiseth [10] presented a sensitivity-based finite element model updating method of a floating bridge and applied it to the Bergsøysund Bridge. Giske et al. [11] proposed a method for estimating the long term extreme responses of floating bridges using the inverse first and second order reliability methods. Junyent et al. [12] investigated the structural responses of floating bridges considering the geometrical nonlinearities associated with fluid structure interaction and large displacements. By using state

space representations for frequency dependent wind and wave forces, Xu et al. [13] developed a time domain method to simulate the dynamic behavior of a three-span suspension bridge with two floating pylons. Sha and Amdahl [14] analyzed the ship collision of a floating bridge considering two scenario, i.e. ship-pontoon and ship-girder collisions. Local structural deformation and damage and global bridge responses were both simulated and analyzed.

Currently, the Norwegian Public Roads Administration (NPRA) is developing the Coastal Highway E39 ferry-free project, in which the deep and wide fjords are to be connected by bridges. These fjords can have a width up to 6 km and a depth up to 1300 m. Designing a reliable and cost-effective floating bridge crossing a wide and deep fjord is very challenging. One of the challenges is that environmental conditions in the fjord, for instance waves, are inhomogeneous. This might imply different wave spectra, wave directions and phase angles between individual waves along the bridge. However, during the design phase, the wave condition encountered at every point of the floating bridge is commonly assumed to be identical for simplicity. Such a simplification will, of course, introduce uncertainty when estimating the structural responses. Hence it is of great interest to assess the wave load effects of a floating bridge in a fjord considering inhomogeneous wave conditions.

An initial floating bridge concept, which was designed for crossing the Bjørnafjorden for the NPRA [16] , was considered in this study. The floating bridge is end-anchored and curved, and consists of a cable-stayed high bridge part and a floating low bridge part supported by 19 pontoons. Fig. 1(a) depicts this floating bridge. A brief introduction about this floating bridge concept is made by Cheng et al. [15]. A more detailed description is presented by COWI [16].

In the initial design of this floating bridge concept, the wave field in Bjørnafjorden was assumed to be homogeneous. Considering a point in the wave field, the wave elevation at this point can be decomposed into a number of wave components with different frequency and direction. For each frequency component in each direction, the wave elements at two different points would have only a deterministic phase difference and amplitude difference. If the phase difference is

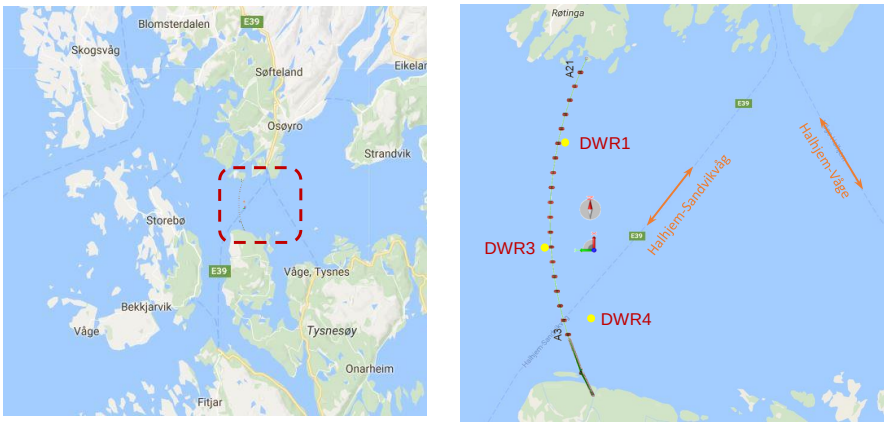

(a) The Bjørnafjorden (b) Floating bridge

Figure 1: (a) Potential site for floating bridge in Bjørnafjorden. (b) An end-anchored curved floating bridge model across the Bjørnafjorden. The approximate position of three Datawell Directional Wave Riders (DWRs) is also marked. [15]

constant and the amplitude difference is zero for any frequency component at any two points, this wave field is regarded as homogeneous; otherwise, it is considered inhomogeneous. A more detailed definition of homogeneous and inhomogeneous wave fields is given in Section 3.1. The use of homogeneous wave field was initially chosen because of the earlier implementation and lack of data about the inhomogeneity.

However, due to the complex topography in fjords, the wave field is actually inhomogeneous. To characterize the wave condition in Bjørnafjorden, the NPRA has deployed three Datawell Wave Riders (DWRs) to measure the wave elevation and wave direction. The approximate position of the three DWRs is along the bridge route, as marked in Fig. 1(b). The measured wave data was analyzed by Cheng et al. [17]. It was found that for wave conditions with a significant wave height H_s higher than 0.3 m, the significant wave height, average zero up-crossing period, and wave direction at these three DWRs differ, indicating that the wave field is inhomogeneous.

As shown by [15], the floating bridge considered has a number of eigen-

modes, which can be excited depending on natural frequencies and phase angles of the wave excitation. It is thus of significant importance to asses the effect of wave inhomogeneity and to reveal the associated uncertainty. Currently there are few studies considering the effect of inhomogeneous waves. Wei et al. [18] proposed a frequency-domain numerical method for hydroelastic predictions of floating structures in inhomogeneous wave field conditions based on multi-rigid-body connected by elastic beams. Wei et al. [19] extended this method to a time domain model based on the linear assumption and impulse response function. Wu et al. [20] studied the dynamic responses of very large floating structures near islands and reefs considering complicated geographical environment, where the wave conditions are inhomogeneous due to islands and reefs. Description of wave conditions and associated hydroelastic responses are addressed. However, this method cannot deal with very complicated floating structures, for example the floating bridge shown in Fig. 3, since the high bridge part cannot be well captured by a simple elastic beam model.

In this study, the low and high bridge parts (see Fig. 2) are modeled by using rigid pontoons, bar elements for the cables, and beam elements for the bridge girder, tower and columns. By using the initial floating bridge designed for Bjørnafjorden, this study addressed the wave load effect considering inhomogeneous wave fields. Based on the wave measurement in Bjørnafjorden, a 1-year inhomogeneous wave condition was assumed for each pontoon by using linear interpolation of measurements of three DWRs. The inhomogeneity in 1-year wave condition was fairly weak, and it was then rationally upscaled to achieve a weakly inhomogeneous 100-year wave condition. A 100-year wave condition with stronger inhomogeneity was also considered. The dynamic responses of floating bridges under these 1-year and 100-year homogeneous and inhomogeneous wave conditions were analyzed and compared.

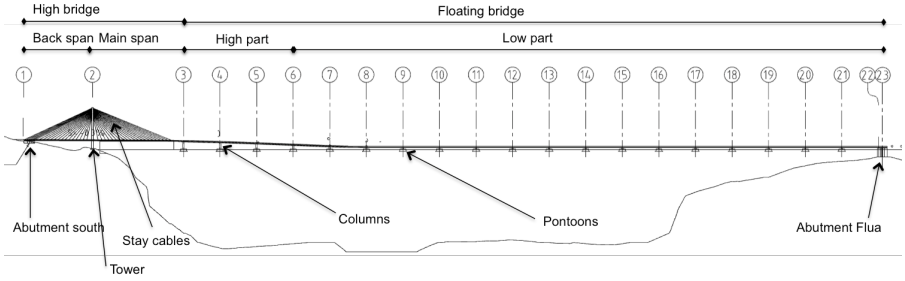

Figure 2: The end anchored curved floating bridge concept [16].

2. Floating bridge concept and numerical model

The concept considered in this study, as shown in Fig. 2, is based on an end-anchored bridge girder curved in the horizontal plane, with a total length of approximately 4600 m and a radius of curvature in the horizontal plane of 5000 m. This bridge concept includes a high bridge part and a low bridge part. The high bridge is cable-stayed located in the south and is designed for ship navigation. It has a main span of 490 m and a back span of 370 m. A total of 80 cables are used to carry the girder. The low bridge part is supported by 19 pontoons with a span of 197 m. The bridge girder is supported by pontoons through columns. The bridge concept is characterized by 23 axis based on location of tower and pontoons, as the numbers marked in Fig. 2.

A numerical model of the floating bridge was built using the coupled codes SIMO/RIFLEX[21, 22], as shown in Fig. 3. SIMO/RIFLEX is codes developed by MARINTEK (now SINTEF OCEAN), in which RIFLEX [21] is a nonlinear finite element solver and SIMO [22] is a solver accounting for various kinds of hydrodynamic loads based on coefficients from a potential flow solver. In the numerical model of the bridge, the girder, tower, columns and cables were modeled as nonlinear flexible elements, while the pontoons were modeled as rigid bodies, as shown in Fig. 4. It should be noted that in the original design, the bridge girder consisted of two parallel steel boxes connected by crossbeams, while in the numerical model, it was simplified as an equivalent beam. The structural properties of typical sections of the bridge girder are given in Table 2,

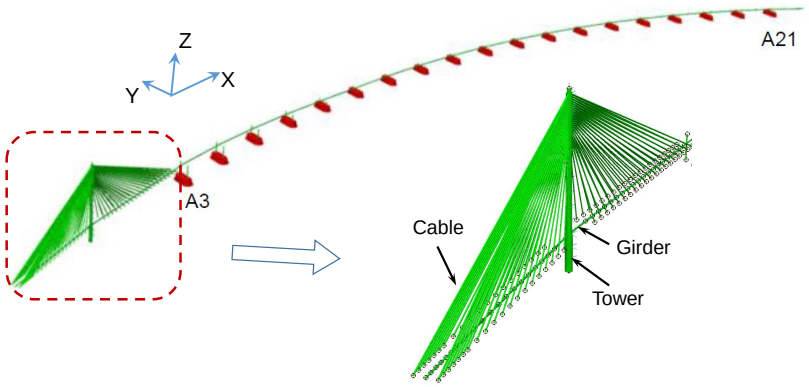

Figure 3: The end-anchored curved floating bridge model including a cable-stayed high bridge and a pontoon-supported low bridge. [15]

in which the location of typical sections are specified in Table 1. Here the detailed properties of the columns, cables and tower are not presented, but they are described in the report by COWI [16, 23].

Table 1: Location of different cross-sectional properties for the bridge girder [16]. Here H1, H2, H3, S1 and F1 represent different cross sections, and the corresponding properties are given in Table 2.

Cross-section	Roadline
Stiff bridge (abutment)	S=0m to S=60m
H1	S=60m to S=220m
H2	S=220m to S=345m
H3	S=345m to S=395m
H2	S=395m to S=520m
H1	S=520m to S=850m
S1	S=850m to S=860m
S1(24.62m) - F1(147.74m) - S1(24.62m)	S=860m to S=4602.74m

Regarding the hydrodynamic modeling, the pontoons were considered as large volume structures and their hydrodynamic coefficients, such as added mass, potential damping and wave excitation forces, were estimated based on potential flow theory. Then convolution technique was applied to estimate the radiation force in time domain based on added mass and potential damping.

Table 2: Structural properties of the bridge girder [16, 23]

		High bridge			Floating bridge	
		H1	H2	H3	S1	F1
Mass	$[ton/m]$	23.96	29.05	33.13	31.8	26.71
EA	$[kN]$	3.07E+08	4.41E+08	5.52E+08	5.25E+08	3.89E+08
EI_z	$[kNm^2]$	1.16E+11	1.70E+11	2.12E+11	2.18E+11	1.55E+11
EI_y	$[kNm^2]$	1.28E+09	1.97E+09	2.46E+09	3.85E+09	2.76E+09
GI_x	$[kNm^2]$	1.42E+09	1.98E+09	2.48E+09	3.70E+09	2.90E+09

Note that I_y and I_z represent the second area moment about the strong axis and weak axis of the girder, respectively. I_x denotes the torsion constant.

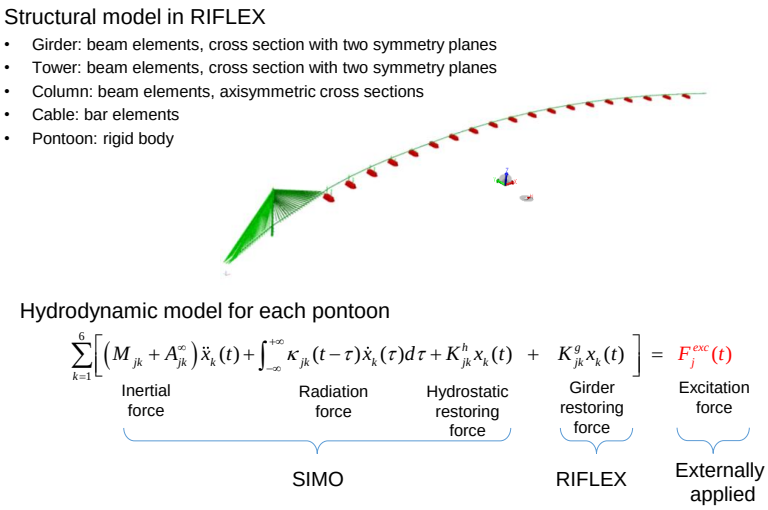

Figure 4: Structural and hydrodynamic modeling of floating bridge. The inhomogeneous wave load effects are accounted for by externally applying the wave excitation force.

The modeling aspects of hydrodynamic loads of this floating bridge were thoroughly addressed by Cheng et al. [15]. It was found that short-crested waves and second order difference-frequency wave loads are very important and were thus considered in this study. The effect of varying water depth at the ends of the bridge can be neglected for this floating bridge. Viscous drag forces can mitigate resonant responses due to second order difference-frequency wave loads.

In addition, the hydrodynamic interaction among pontoons was ignored in this study, because the spacing between two neighboring pontoons are very large, about 197 m, which is more than 4 times typical wave length under 100-year wave condition.

In the numerical model, two ends of the bridge and the tower bottom were fixed. The connection point between the girder and the tower had fixed degree of freedom in transverse direction (sway). Master-slave rigid connection was applied between cable ends and girder, between girder and columns, and between pontoons and columns. The pretension in each cable was also accounted for in the numerical model.

The definitions of rigid body motions of the pontoons are shown in Fig. 5. The strong axis and weak axis of the bridge girder is also highlighted in Fig. 5. The global coordinate system is defined as shown in Fig. 2. X is positive in the north direction, and Y is positive in the west direction. and Z is positive upward. The origin is located at the water plane at the south end. The incoming wave directions are also indicated in Fig. 2.

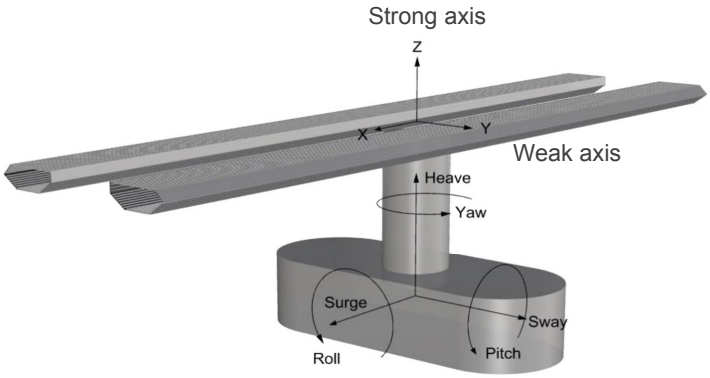

Figure 5: Definition of rigid body motions of the pontoons and the strong and weak axes of the bridge girder [23].

Eigen-frequencies and eigen-modes for this floating bridge were analyzed by Cheng et al. [15]. This floating bridge has a large number of eigen-modes. The

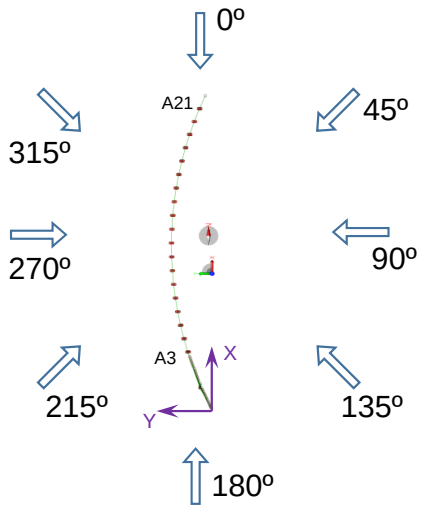

Figure 6: Definition of global coordinate system and wave incoming directions. [15]

eigen-periods and dominant motions for the first four modes are given in Table 3 and the corresponding eigen-modes are plotted in Fig. 7. The first two eigen periods are 55.5 s and 31.8s, which correspond to a dominant motion in horizontal plane. These two modes are likely to be excited by second order difference frequency wave loads. There are about 20 eigen-modes that are dominated by vertical motions. They have a eigen-period ranging from 7.47 s to 11.48 s, which are due to heave motion of pontoons. For eigen-modes with a eigen-period ranging from 3.7 s to 7 s, the dominating motions are mainly torsional motions. More than 25 eigen-modes have a eigen-period below 3.7 s, in which the dominating motions are mainly pendulum motions, because of surge motion of pontoons.

3. Methodology

3.1. Wave field in a fjord

The characteristics of wave field in a fjord have been described by Cheng et al. [15]. The waves are likely to be short crested, consisting of local wind

Table 3: The first four eigen periods of the floating bridge model.

Mode	Period [16]	Frequency [16]	Period	Error	Dominant motions	
	[s]	[rad/s]	[s]	[%]	Primary motion	Secondary motion
1	56.72	0.111	55.52	2.12	Sway	Surge
2	31.69	0.199	31.81	-0.38	Sway	Surge
3	22.68	0.277	23.07	-1.72	Sway	Torsion
4	18.62	0.337	19.04	-2.26	Sway	Surge

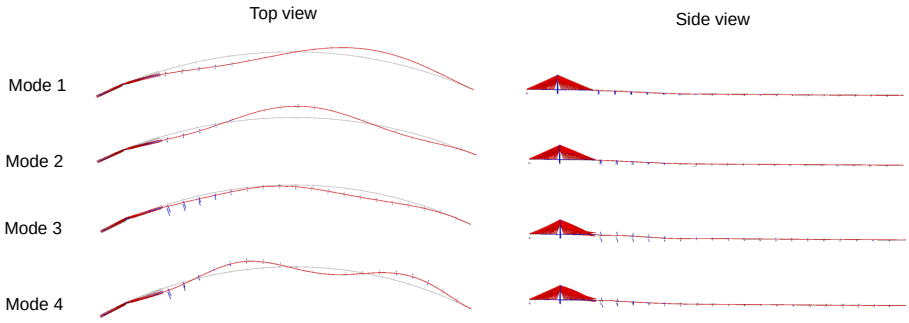

Figure 7: Several selected eigen-modes of the floating bridge based on eigen-value analysis by the SIMO/RIFLEX codes [15].

generated waves and possible swell from the ocean. For Bjørnafjorden, the waves are mainly generated by local winds and are short crested.

To characterize the wave condition in Bjørnafjorden, both field measurements and numerical simulations have been conducted by the NPRA. The measured time series of wave data has been analyzed by Cheng et al. [17]. The locations of DWR1, DWR3, and DWR4 are highlighted in Fig. 1(b), which are approximately corresponding to the pontoons at A17, A9 and A3, respectively. Fig. 8 depicts the directional wave spectrum measured at DWR3 based on Extended Maximum Likelihood Method (EMLM) for the case with highest significant wave height. It can be clearly observed that the waves are short crested and has a principle wave direction θ_p. Table 4 gives the measured wave condition at the three DWRs when the largest significant wave height was recorded. It can be found that wave conditions at three DWRs differ, especially with respect to significant wave height and principle direction. In other words, the wave field

185 in Bjørnafjorden is inhomogeneous.

Table 4: The measured sea state with largest wave in 1 year

	H_s [m]	T_p [s]	θ_p[°]
A3 (DWR4)	1.1	3.77	312
A9 (DWR3)	1.12	3.77	305
A17 (DWR1)	1.22	3.77	288

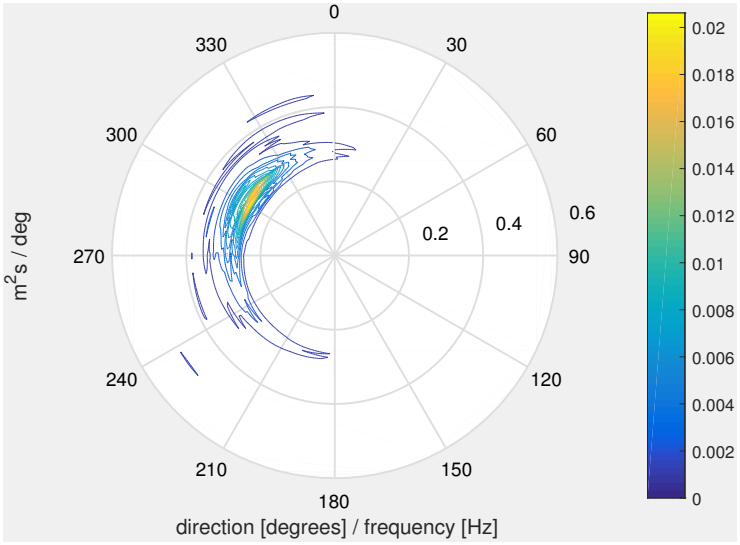

Figure 8: The directional wave spectra estimated at DWR3 by Extended Maximum Likelihood Method (EMLM) for the case with highest significant wave height. [17]

Numerical simulations were carried out by Norconsult [24], separately dealing with the swell and wind generated waves. They were based on the phase-averaged energy balanced equation, which provides wave spectra, but not time series of the wave elevation. It was revealed that swell is fairly small and wind
190 generated waves are extremely dominating. Based on hindcast wind data in Bjørnafjorden from 1979 to 2015, the 100-year wind waves were estimated, as given in Table 5. Nevertheless, the distributions of significant wave height and peak period over the fjord are not provided in this table, which implies that the inhomogeneity of the 100-year wave condition is thus not known. The inhomo-

Table 5: 100-year wind waves in Bjørnafjorden based on numerical simulations [25]

Sectors	H_s [m]	T_p [s]
345°- 75°	1.5	5.0
75° - 105°	2.8	6.6
105° - 165°	1.6	5.3
165° - 225°	1.9	5.3
225° - 315°	2.4	5.9
315° - 345°	2.5	6.2

geneous waves under 100-year wave condition should be reasonably assumed.

3.2. Description of short-term homogeneous and inhomogeneous wave field

In this study, the short-term wave conditions are considered. The wave elevation is modeled by linear superposition of all wave components from different directions, as follows

$$\zeta(x,y,t) = \Re \sum_{n=1}^{N} \sum_{m=1}^{M} \sqrt{2S_\zeta(\omega_n,\theta_m)\Delta\omega\Delta\theta}\exp\left[i\left(\omega_n t - k_n x\cos(\theta_m) - k_n y\sin(\theta_m) + \epsilon_{nm}\right)\right] \tag{1}$$

Here N and M are the total number of wave frequency components and wave direction components respectively. ϵ_{nm} is the random phase angle uniformly distributed within $[0, 2\pi)$, x and y are the coordinates of the floater, θ is wave direction angle, and k is wave number and is related to the wave frequency through the dispersion relation. $S_\zeta(\omega,\theta)$ denotes the directional wave spectrum and is a function of frequency and wave direction.

$$S_\zeta(\omega,\theta) = S(\omega)D(\theta) \tag{2}$$

in which the wave spectrum $S(\omega)$ is modeled by the JONSWAP spectrum and the directional distribution $D(\theta)$ takes the cos-s distribution [26].

$$D(\theta) = \frac{\Gamma(1+s/2)}{\sqrt{\pi}\Gamma(1/2+s/2)}\cos^s(\theta-\theta_p) \tag{3}$$

where θ_p is the principle wave direction, s is the spreading exponent and is set to be 4 for short-crested waves [25]. Two representative wave spectra of the 1-year and 100-year wave conditions used in this study are demonstrated in Fig. 9.

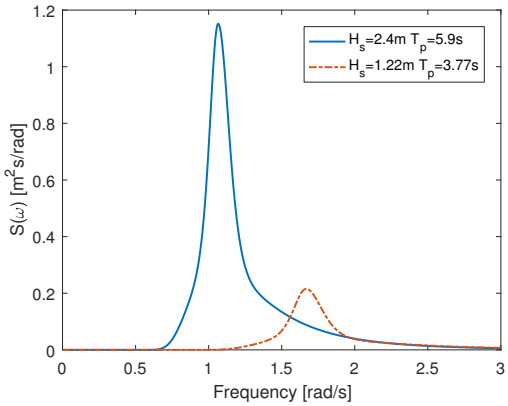

Figure 9: Representative wave spectra for the 1-year and 100-year wave conditions.

Hence, the wave elevation at point (x, y) is related to wave spectrum $S(\omega)$, directional distribution $D(\theta)$, and random phase angle ϵ_{nm}. When the types of wave spectrum and directional distribution are determined, the wave elevation at point (x, y) can be regarded as a function of significant wave height H_s, peak period T_p, principle wave direction θ_p and random phase angle ϵ_{nm}. For the floating bridge considered in this study, the wave field is homogeneous if these four parameters are identical for all pontoons; otherwise, the wave field is considered inhomogeneous.

In numerical simulations, the random phase angle ϵ_{nm} is controlled by a random seed number. By specifying the significant wave height H_s, peak period T_p, principle wave direction θ_p and random seed number, the current version of SIMO itself can generate the time series of wave elevations at each pontoon for numerical analyses. In this sense, the wave parameters (H_s, T_p, θ_p and ϵ_{nm}) specified for each pontoon are identical, implying that SIMO can account for homogeneous wave conditions. To extend the capability of SIMO to account for inhomogeneous wave conditions and wave load effects, a possible approach is to generate the time series of wave elevation at each pontoon externally so as to adjust the wave parameters (H_s, T_p, θ_p and ϵ_{nm}) separately for each pontoon. Based on this approach, the method that can account for inhomogeneous wave load effects is proposed in the next section.

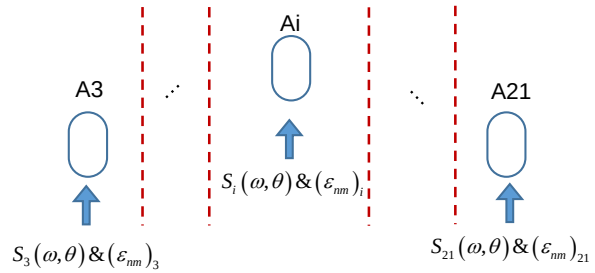

$S_i(\omega,\theta)$: Directional wave spectra for pontoon at Ai, is a function of (H_s,T_p,θ_p)

$(\varepsilon_{nm})_i$: Random phase angle for pontoon at Ai

Homogeneous wave condition:

$$i,j\in[3,21]\&i\neq j \qquad (H_s,T_p,\theta_p,\varepsilon_{nm})_i=(H_s,T_p,\theta_p,\varepsilon_{nm})_j$$

Inhomogeneous wave condition:

$$i,j\in[3,21]\&i\neq j \qquad (H_s,T_p,\theta_p,\varepsilon_{nm})_i\neq(H_s,T_p,\theta_p,\varepsilon_{nm})_j$$

Figure 10: Description of homogeneous and inhomogeneous wave fields

3.3. A method accounting for inhomogeneous wave load effect

In SIMO, each pontoon was modeled as a rigid body and the dynamics of the pontoon can be represented using the equation of motion proposed by [27]

$$\sum_{k=1}^{6}\left[\left(M_{jk}+A_{jk}^{\infty}\right)\ddot{x_k}(t)+\int_{-\infty}^{\infty}\kappa_{jk}(t-\tau)\dot{x_k}(\tau)\,d\tau+\left(K_{jk}^{g}+K_{jk}^{h}\right)x_k(t)\right]=F_j^{exc}(t) \tag{4}$$

where j and k are degree of freedom $(j,k=1,2,...,6)$, M_{jk} is the mass of the pontoon, A_{jk}^{∞} is the infinite frequency added mass, $x_k(t)$, $\dot{x_k}(t)$ and $\ddot{x_k}(t)$ are the displacement, velocity and acceleration of the pontoon, respectively. $\kappa_{jk}(t-\tau)$ is the retardation function which represents the fluid memory effect. K_{jk}^{h} is the hydrostatic restoring and K_{jk}^{g} is the nonlinear restoring resulting from the bridge girder. $F_j^{exc}(t)$ is the excitation forces which includes the first order wave forces $F_j^{1}(t)$, second order mean and slowly varying wave drift forces $F_j^{2}(t)$ and viscous drag forces $F_j^{Drag}(t)$.

$$F_j^{exc}(t)=F_j^{1}(t)+F_j^{2}(t)+F_j^{Drag}(t) \tag{5}$$

In Eq. 4, only the right hand side of the equation, i.e. the wave excitation force $F_j^{exc}(t)$, is related to the incident wave condition. The first-order wave forces and second-order wave forces can be expressed as a function of wave force transfer function and wave elevation. The viscous drag forces are due to relative velocities between water particles and the floater. In this study, the viscous drag forces are not considered, but the effect of viscous drag forces on the dynamics of the floating bridge was studied by Cheng et al. [15].

To account for the inhomogeneous wave loads, $F_j^{exc}(t)$ should be applied separately for each pontoon. This can be achieved in SIMO by assuming calm water and by applying the wave excitation forces as external forces separately for each pontoon. In this case, the time series of wave excitation forces should be pregenerated given a sea state. The generation of first-order and second-order wave excitation forces has been addressed by Cheng et al. [15] and is thus not given here.

4. Load cases and environmental conditions

In this study, a series of load cases (LCs) were defined to investigate the wave load effect on the dynamics of the floating bridge under homogeneous and inhomogeneous wave conditions.

LC1 considers 1-year wave condition. The measured wave condition with the largest significant wave height at three DWRs is given in Table 4. The locations of DWR1, DWR3 and DWR4 approximately correspond to the pontoons at A17, A9 and A3 (see Fig. 1(b)), respectively. Since the pontoons are equally spaced, the wave conditions at A3-A17 can be obtained by linear interpolation with respect to H_s, T_p, and θ_p. Wave conditions at A18-A21 can also be approximated when assuming the wave condition at A21. Therefore, the 1-year inhomogeneous wave condition can be approximately obtained, as given in Table 6. Based on these 1-year inhomogeneous wave conditions, LC1 is defined as

- LC1.1: Homogeneous 1-year wave condition. For all pontoons, $H_s = 1.22$

m , T_p = 3.77 s, θ_p = 288°, and random phase angles of each wave component in Eq. 1 are identical.

- LC1.2: Inhomogeneous 1-year wave condition. For all pontoons, H_s = 1.22 m , T_p = 3.77 s, θ_p = 288°, and random phase angles of each wave component in Eq. 1 are different.

- LC1.3: Inhomogeneous 1-year wave condition. Wave parameters for each pontoon are given in Table 6. The random phase angle of each wave component in Eq. 1 is identical for all pontoons.

- LC1.4: Inhomogeneous 1-year wave condition. Wave parameters for each pontoon are given in Table 6. The random phase angle of each wave component in Eq. 1 is different for each pontoon.

The dynamic responses of the floating bridge in a 100-year wave condition is also of interest and is considered in LC2 and LC3. The 100-year wave condition in Bjørnafjorden has been numerically simulated for each direction and described in the metocean design bases [25], as given in Table 5. According to the metocean design basis, the 100-year wave condition that comes from Northwest is H_s = 2.4 m and T_p = 5.9 s. However, the wave inhomogeneity for 100-year wave conditions is currently not available. Therefore, to reasonably represent the 100-year inhomogeneous wave condition, the following assumptions are made

- the inhomogeneity in terms of significant wave height under 100-year wave condition is consistent with that of 1-year wave condition,

- the peak period at each pontoon is the same,

- the principle wave direction is the same as those in the 1-year inhomogeneous wave condition.

Similarly, based on these 100-year inhomogeneous wave conditions, LC2 is defined as

Table 6: The 1-year and 100-year inhomogeneous wave condition

	LC1:1-year wave cond.			LC2:100-year wave cond.			LC3:100-year wave cond.		
	H_s	T_p	θ_p	H_s	T_p	θ_p	H_s	T_p	θ_p
A3	1.100	3.77	312.0	2.164	5.9	312.0	1.6	5.9	315.0
A4	1.103	3.77	310.8	2.170	5.9	310.8	1.6	5.9	315.0
A5	1.107	3.77	309.7	2.177	5.9	309.7	1.6	5.9	315.0
A6	1.110	3.77	308.5	2.183	5.9	308.5	1.6	5.9	315.0
A7	1.113	3.77	307.3	2.190	5.9	307.3	2	5.9	300.0
A8	1.117	3.77	306.2	2.196	5.9	306.2	2	5.9	300.0
A9	1.120	3.77	305.0	2.203	5.9	305.0	2	5.9	300.0
A10	1.121	3.77	302.9	2.206	5.9	302.9	2	5.9	300.0
A11	1.123	3.77	300.8	2.208	5.9	300.8	2	5.9	300.0
A12	1.124	3.77	298.6	2.211	5.9	298.6	2	5.9	300.0
A13	1.125	3.77	296.5	2.213	5.9	296.5	2.4	5.9	285.0
A14	1.126	3.77	294.4	2.216	5.9	294.4	2.4	5.9	285.0
A15	1.128	3.77	292.3	2.218	5.9	292.3	2.4	5.9	285.0
A16	1.129	3.77	290.1	2.220	5.9	290.1	2.4	5.9	285.0
A17	1.220	3.77	288.0	2.400	5.9	288.0	2.4	5.9	285.0
A18	1.193	3.77	283.5	2.347	5.9	283.5	2.4	5.9	285.0
A19	1.167	3.77	279.0	2.295	5.9	279.0	2	5.9	270.0
A20	1.140	3.77	274.5	2.242	5.9	274.5	2	5.9	270.0
A21	1.110	3.77	270.0	2.184	5.9	270.0	2	5.9	270.0

- LC2.1: Homogeneous 100-year wave condition. For all pontoons, H_s = 2.4 m , T_p = 5.9 s, θ_p = 288°, and random phase angles of each wave component in Eq. 1 are identical.

- LC2.2: Inhomogeneous 100-year wave condition. For all pontoons, H_s = 2.4 m , T_p = 5.9 s, θ_p = 288°, and random phase angles of each wave component in Eq. 1 are different.

- LC2.3: Inhomogeneous 100-year wave condition. Wave parameters for each pontoon are given in Table 6. The random phase angle of each wave component in Eq. 1 is identical for all pontoons.

- LC2.4: Inhomogeneous 100-year wave condition. Wave parameters for each pontoon are given in Table 6. The random phase angle of each wave

component in Eq. 1 is different for each pontoon.

The inhomogeneity described in LC2 is fairly weak, since the variation of significant wave height is very small, within 10% of the maximum significant wave height. To distinctly reveal the effect of inhomogeneous waves, LC3 with stronger inhomogeneity is assumed, as given in Table 6. LC3 divides the pontoons into several groups and enlarges the variations of significant wave heights and principle wave directions among each group. The peak period for each pontoon is still held constant. Similarly, two sub-cases are defined for LC3, as follows:

- LC3.1: Inhomogeneous 100-year wave condition. Wave parameters for each pontoon are given in Table 6. The random phase angle of each wave component in Eq. 1 is identical for all pontoons.

- LC3.2: Inhomogeneous 100-year wave condition. Wave parameters for each pontoon are given in Table 6. The random phase angle of each wave component in Eq. 1 is different for each pontoon.

All the above inhomogeneous wave conditions considered are based on two limiting cases, i.e. identical or different random phase angles of each wave component for all pontoons. In reality, random phase angles of each wave component for all pontoons are not likely to be totally identical or different. The wave condition is likely to be within these two limiting cases. It should also be noted that for each LC, 10 identical and independent simulations were carried out. It is used to reduce the stochastic variation of dynamic responses. The statistical values and spectra presented in the following sections are based on the average of 10 seeds for each LC. In addition, since the 1-year wave condition is established based on measurements within about eight months, large uncertainty might exist; as a result, the 100-year wave condition has a significant wave height of 2.4 m, which is about twice that of 1-year wave condition.

5. Results and discussion

5.1. Inhomogeneous wave load effects in LC1 under 1-year wave condition

In this section, the inhomogeneous wave load effects on the dynamics of floating bridge were studied under the 1-year wave condition. The 1-year inhomogeneous wave conditions are based on the measurements in the fjord, as the LC1 defined in Section 4. LC1.1 is homogeneous wave condition while LC1.2, LC1.3 and LC1.4 are inhomogeneous wave conditions. The waves were modeled as short crested waves and the second order difference-frequency wave loads were considered.

Mean values of the dynamic responses of the floating bridge are first analyzed. The difference in the mean values of sway motion along the bridge girder between LC1.1, LC1.2, LC1.3 and LC1.4 is within 1 cm, which is negligible. The differences in the mean values of axial force, and strong axis bending moment M_y are respectively less than 150 kN and 150 kNm, which are also very small compared to the mean value. The mean value of weak axis bending moment M_x is almost identical for these three cases. Therefore, the mean values of dynamic responses of the floating bridge are not sensitive to the inhomogeneous waves. Hereinafter, analyses and discussions mainly focus on the dynamic part of the responses of the floating bridge.

The sway motion along the bridge girder is investigated by analyzing the standard deviation and power spectra. Fig. 11(a) presents the standard deviation of sway motion along the bridge girder in LC1. Overall, the inhomogeneous wave case LC1.2 gives the largest standard deviation of sway motion along the bridge. The inhomogeneous wave cases LC1.3 and LC1.4 cause smaller sway standard deviation in the vicinity of A11 than the homogeneous wave case LC1.1. However, at other parts of the low bridge, the sway standard deviation in the inhomogeneous wave cases is larger, especially for LC1.2 and LC1.4; in other words, the variation of sway standard deviation along bridge girder in the inhomogeneous wave cases is severer than that in the homogeneous wave case.

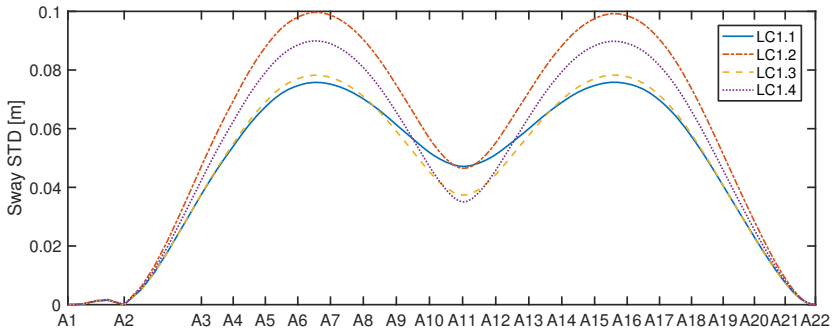

(a) Sway STD

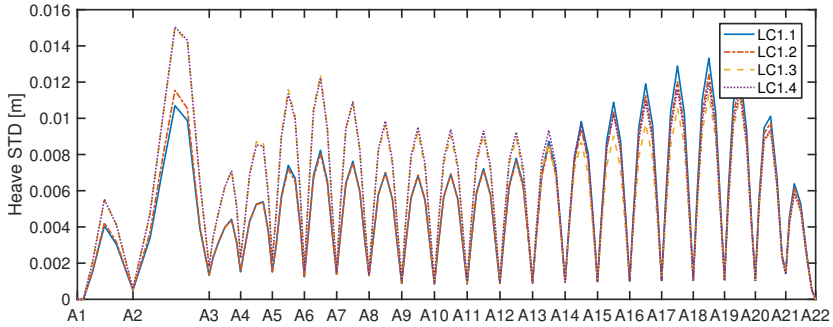

(b) Heave STD

Figure 11: The standard deviation of sway and heave motions along the bridge girder under 1-year wave condition.

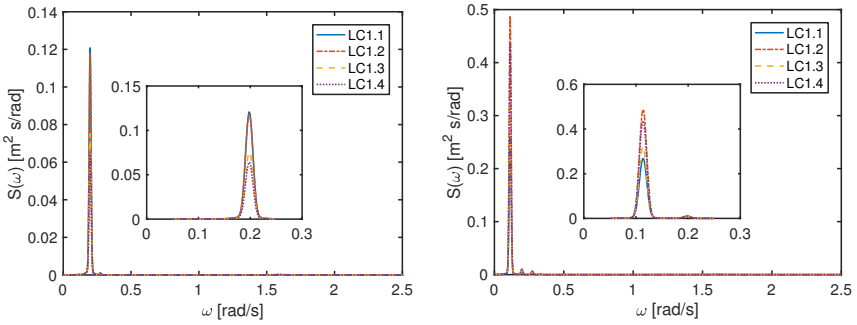

(a) At A11 (b) At A16

Figure 12: Spectra of sway motion of girder nodes at (a) A11, (b) A16 under 1-year wave condition.

To further reveal the reasons for discrepancies in sway standard deviation, power spectral analysis is carried out at two selected points, as shown in Fig. 12. For all four cases in LC1, the sway response at A11 is dominant by the second mode resonant response, and at A16 the first mode resonant response is more dominating. As the node moves from A11 to A16, the first mode resonant response increases, and on the contrary the second mode resonant response gradually decreases. In addition, at A11 LC1.1 and LC1.2 have a much larger second mode resonant response than LC 1.3 and LC1.4, while at A16 LC1.2 and LC1.4 arise a significantly larger first mode resonant response than LC1.1 and LC1.3. The difference between LC1.1 and LC1.4 at A6 and A16 is larger than that at A11, the reason is owing to the extent to which the resonant eigen-modes are excited.

The standard deviation of heave motion is shown in Fig. 11(b). Inhomogeneous wave cases LC1.3 and LC1.4 give large heave standard deviation for girders between A1 to A13, while for girders ranging from A13 to A22, homogeneous wave cases cause larger heave standard deviation. To figure out reasons for these difference, power spectra of heave motion at A6 and A16 are analyzed and shown in Fig. 13. At A6, the inhomogeneous waves, especially LC1.3, excite stronger resonant heave motions at frequency of 0.57 rad/s and at frequencies ranging from 1.2 rad/s to 1.8 rad/s. However, at A16, the wave frequency response and associated resonant responses are very dominant for these four LCs; the LC1.1 has a slightly larger significant wave height, and consequently it arises a little larger heave standard deviation.

The standard deviation of axial force along the bridge girder is shown in Fig. 14. In general, the axial force along the bridge girder is quite close between LC1.3 and LC1.4, and between LC1.1 and LC1.2. The inhomogeneous wave cases LC1.3 and LC1.4 cause a bit smaller standard deviation of axial force for girders at A10-A15 than LC1.1 and LC1.2, while for other girders, the axial force in LC1.3 and LC1.4 is larger, and the difference can reach up to approximately 20%. In addition, distinct resonant modes and responses are identified by power spectral analyses, as shown in Fig. 15. At both A6 and A16, primary resonant

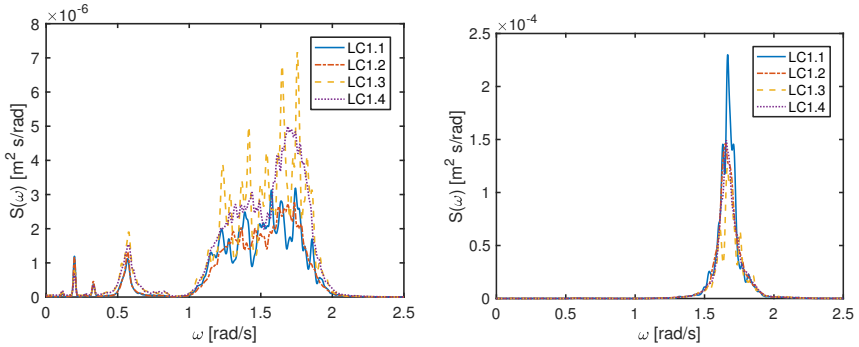

(a) at A6 (b) at A16

Figure 13: Spectra of heave motion of girder nodes at (a) A6 and (b) A16 under 1-year wave condition.

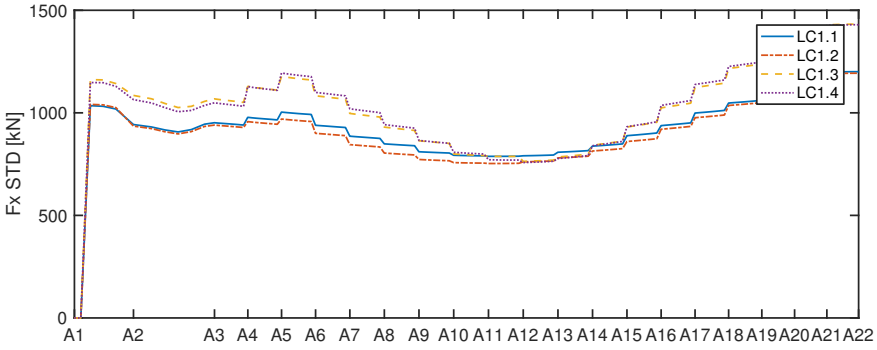

Figure 14: The standard deviation of axial force F_x along the bridge girder under 1-year wave condition.

responses corresponding to the second and third resonant modes are observed and LC1.1 gives larger resonant responses in these two modes. However, the wave frequency responses and associated resonant responses in the vicinity of wave frequencies are larger for LC1.3 and LC1.4.

The standard deviation of strong axis bending moment M_z, weak axis bending moment M_y and torsional moment M_x along the bridge girder are presented in Fig. 16. Compared to M_z, M_y and M_x are more sensitive to inhomogeneous wave conditions. M_y in LC1.3 and LC1.4 is very close, and for girders between A3 and A12, M_y in LC1.3 and LC1.4 is much larger than M_y in LC1.1. Differ-

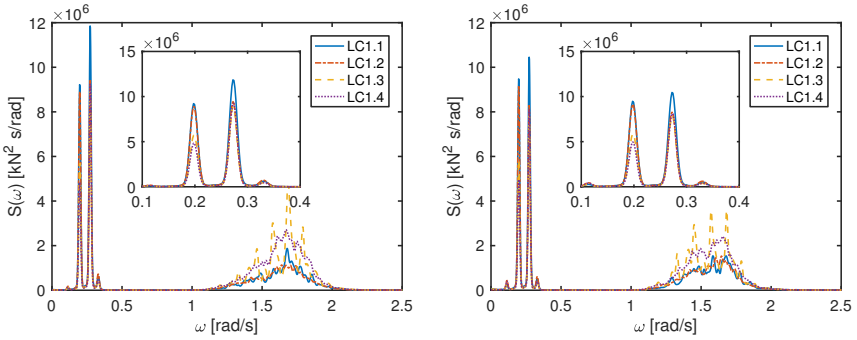

(a) at A6 (b) at A16

Figure 15: Spectra of axial force F_x of girder nodes at (a) A6 and (b) A16 under 1-year wave condition.

ence between inhomogeneous wave cases and homogeneous wave case can reach up to about 80%. Additionally, power spectral analysis of M_y in these girders, as shown in Fig. 17(b), indicates that wave frequency responses and associated resonant responses in the vicinity of wave frequencies are dominant.

Regarding the torsional moment M_x, its standard deviation gradually increases from A1 to A7, and holds small variation in other parts. Similar as M_y, the response of M_x is dominated by wave frequency responses and associated resonant responses in the vicinity of wave frequencies. A number of modes dominated by torsion motion is located in this range [15].

To summarize, compared to the homogeneous wave case LC1.1, inhomogeneous wave cases LC1.2, LC1.3 and LC1.4 can cause larger responses with respect to sway and heave motions, axial force and weak axis bending moment.

5.2. Inhomogeneous wave load effects in LC2 under 100-year wave condition

The 1-year wave condition analyzed in the above section induces relatively small bridge motion, as the maximum sway standard deviation is less than 0.09 cm. In this section, the 100-year wave condition in LC2 is analyzed, and larger responses are induced.

The standard deviations of sway and heave motions in LC2 under 100-year

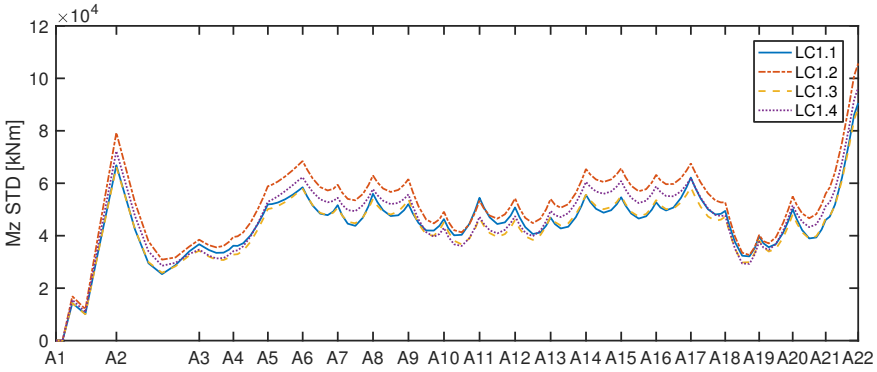

(a) Moment about bridge girder strong axis, M_z

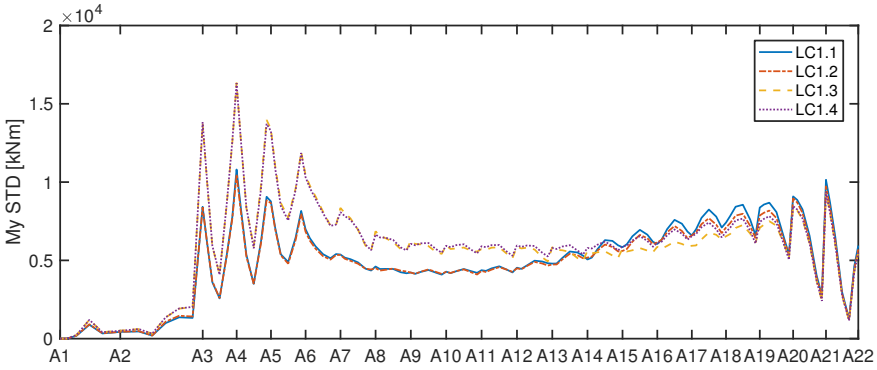

(b) Moment about bridge girder weak axis, M_y

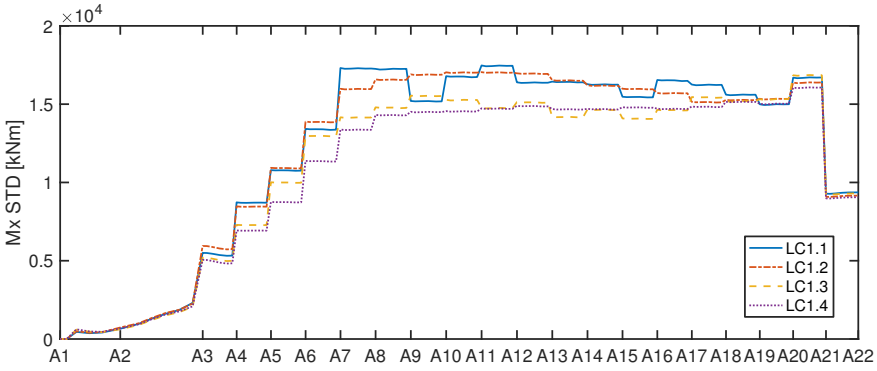

(c) Torsion moment, M_x

Figure 16: The standard deviation of (a) moment about bridge girder strong axis M_z, (b) moment about bridge girder strong axis M_y, and (c) torsion moment M_x along the bridge girder under 1-year wave condition.

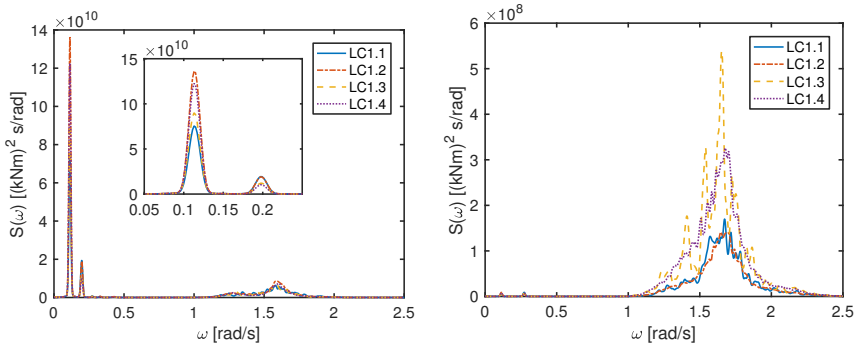

(a) Strong axis bending moment, M_z (b) Weak axis bending moment, M_y

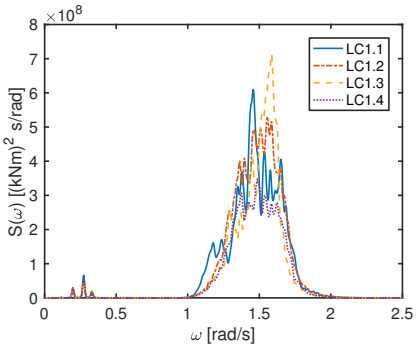

(c) Torsion moment, M_x

Figure 17: The power spectra of (a) moment about bridge girder strong axis M_z, (b) moment about bridge girder strong axis M_y, and (c) torsion moment M_x of girder node at A6 under 1-year wave condition.

wave condition are plotted in Fig. 18. The variation of sway standard deviation along the bridge girder in LC2 is quite similar to that in LC1. But the value of sway standard deviation in LC2 is more than 4 times larger than those in LC1. Additionally, power spectral results demonstrated in Fig. 19 indicate that the resonant modes induced at each node along the bridge girder in LC2 is also similar to those in LC1, as shown in Fig. 12.

The heave standard deviation in LC2, as plotted in Fig. 18(b), presents evident discrepancies compared to that in Fig. 11(b) in LC1. Reasons for such discrepancies are revealed by power spectral analysis. In LC2, resonant modes

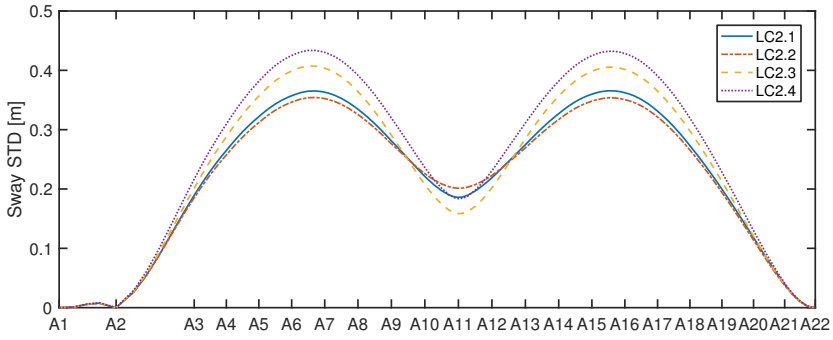

(a) Sway STD

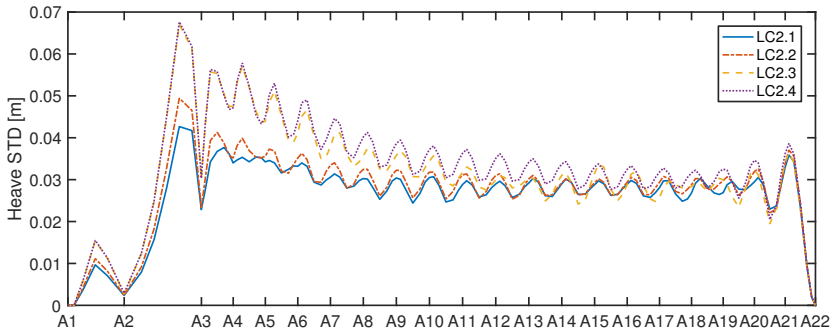

(b) Heave STD

Figure 18: The standard deviation of sway and heave motions along the bridge girder under 100-year wave condition in LC2.

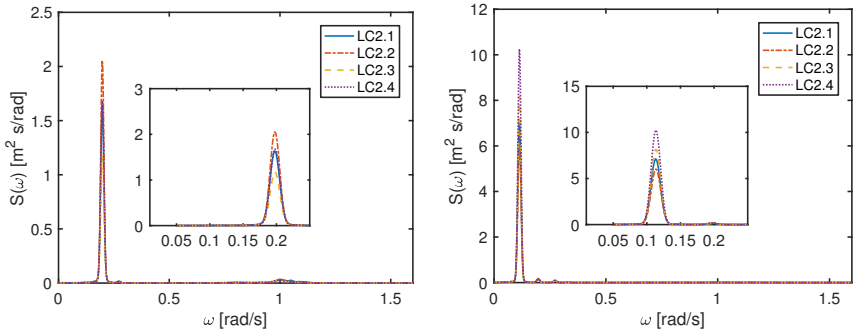

(a) At A11 (b) At A16

Figure 19: Spectra of sway motion of girder nodes at (a) A11, (b) A16 under 100-year wave condition in LC2.

corresponding to a frequency of 0.82 rad/s are excited to cause larger heave motions. Moreover, a resonant mode with a frequency of 0.72 rad/s is excited at A16. These resonant responses dominate heave motion in LC2, while in LC1 the heave motion is dominant by wave frequency responses and associated resonant responses around wave frequencies.

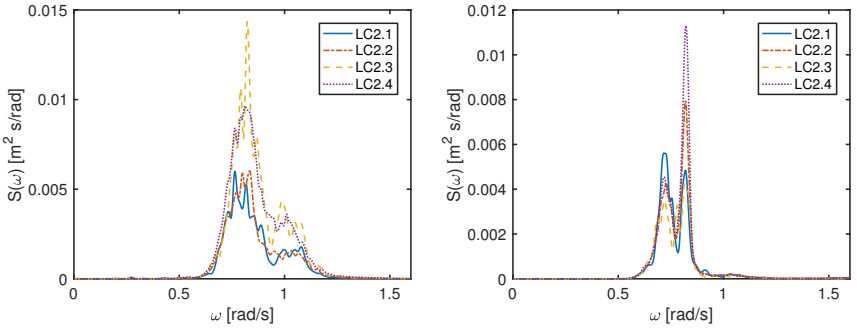

(a) At A4 (b) At A16

Figure 20: Spectra of heave motion of girder nodes at (a) A4 and (b) A16 under 100-year wave condition in LC2.

The variation of standard deviation of axial force F_x along the bridge girder in LC2 , as shown in Fig.21(a), follows similar trend as that in LC1, as shown in Fig. 14. So does the strong axis bending moment M_z. But the values of F_x and M_z in LC2 are several times larger than those in LC1. Power spectra results of F_x and M_z along the bridge girder are also analyzed, and an example of power spectra of F_x and M_z of girder node at A16 is plotted in Fig. 22. Compared with those in LC1, similar resonant modes are excited in LC2.

Contrary to F_x and M_z, the standard deviations of torsional moment M_x and weak axis bending moment M_y in LC2 are different from those in LC1. Fig. 23 presents the standard deviation of M_x and M_y along the bridge girder and power spectra of M_x and M_y of girder node at A6 are plotted in Fig. 24. The homogeneous wave case LC2.1 overestimate M_x at certain parts of girder, and underestimate it at other parts. The notable difference is located at girders between A5 to A7, where the maximum overestimation is about 44%. In addi-

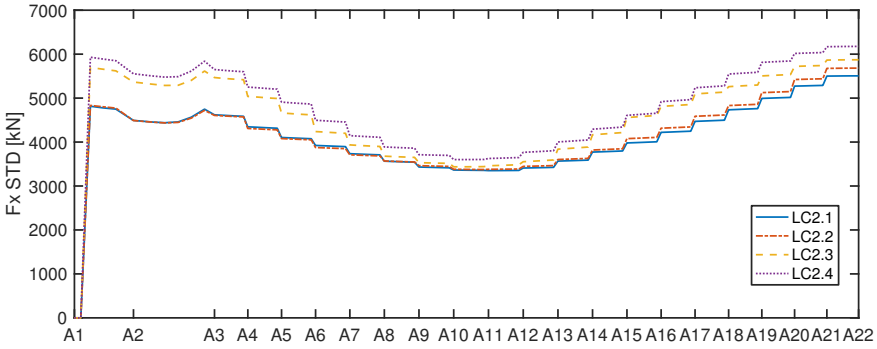

(a) Axial force, F_x

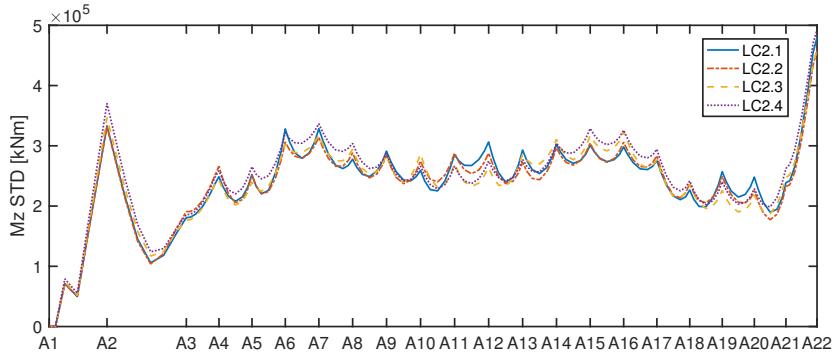

(b) Strong axis bending moment, M_z

Figure 21: The standard deviation of axial force F_x along the bridge girder under 100-year wave condition LC2.

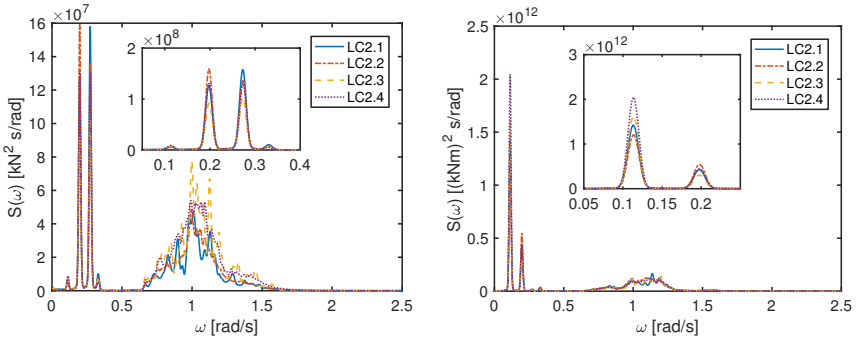

(a) Axial force, F_x (b) Strong axis bending moment, M_z

Figure 22: Spectra of axial force F_x and strong axis bending moment M_z of girder nodes at A16 under 100-year wave condition LC2.

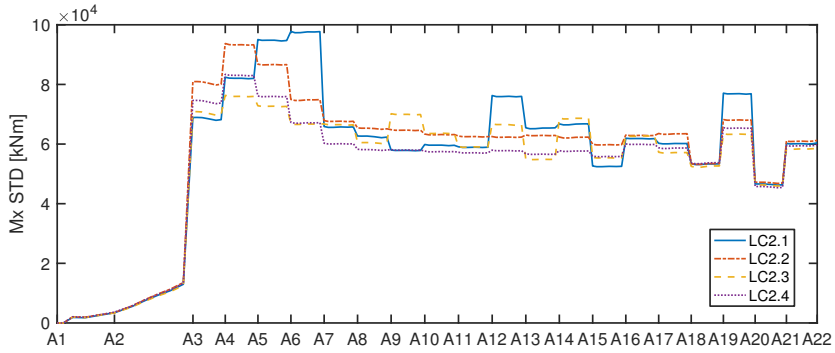

(a) Torsion moment, M_x

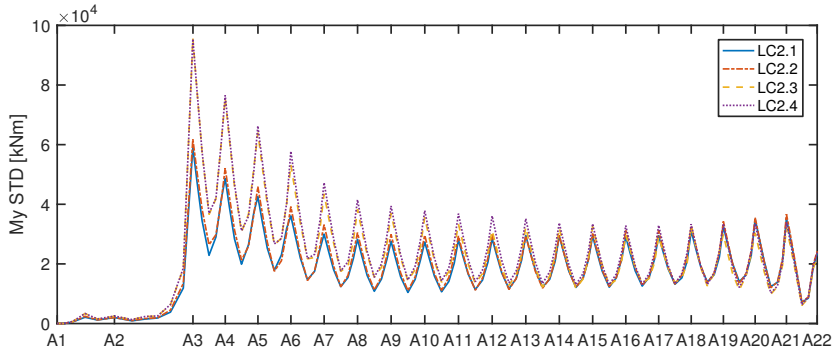

(b) Weak axis bending moment, M_y

Figure 23: The standard deviations of (a) torsion moment M_x, and (b) moment about bridge girder strong axis M_y along the bridge girder under 100-year wave condition LC2.

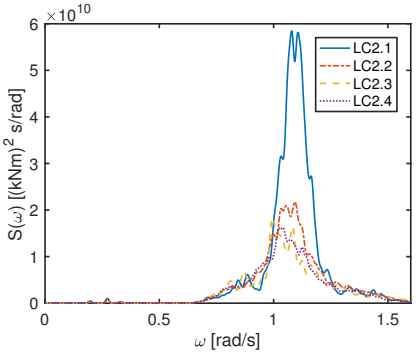

(a) Torsion moment, M_x

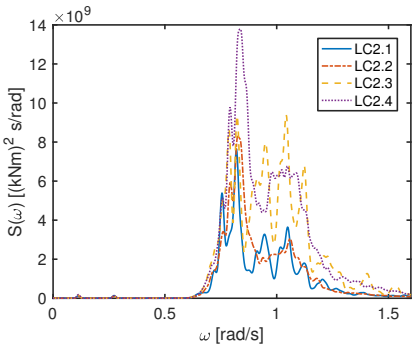

(b) Weak axis bending moment, M_y

Figure 24: Spectra of weak axis bending moment M_z and torsion moment M_x of girder nodes at A6 under 100-year wave condition LC2.

tion, the power spectrum of M_x is mainly dominant by wave frequency responses and associated resonant responses around wave frequencies.

The homogeneous wave case LC2.1 greatly underestimates M_y for girders between A3 and A10, and this underestimation can reach 60% at A3. Power spectral analysis in Fig. 24(b) shows that this is because inhomogeneous wave cases LC2.3 and LC2.4 excite several stronger resonant responses with frequency ranging from 0.76 rad/s to 1.12 rad/s.

5.3. Inhomogeneous wave load effects in LC3 under 100-year wave condition

The wave condition used in LC2 is weakly inhomogeneous, since the significant wave heights for each pontoon are fairly close. In this section, stronger inhomogeneous wave condition, i.e. LC3, is considered. The results are also compared to the homogeneous wave condition LC2.1, and the inhomogeneous wave condition LC2.2.

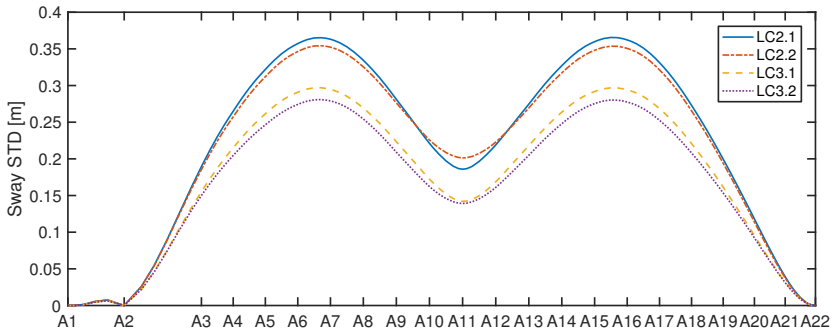

Figure 25: The standard deviation of sway motion along the bridge girder under 100-year wave condition in LC3.

Fig. 25 presents the standard deviation of sway motion along the bridge girder in LC2.1, LC2.2 and LC3. Compared to those results in LC2 shown in Fig. 18, inhomogeneous wave conditions (LC3) give much smaller standard deviation in sway motion than homogeneous wave condition (LC2.1). It indicates that though the inhomogeneity in LC3 is stronger than those in LC2.3 and LC2.4, the sway motion is otherwise smaller. The reasons are revealed by power spectral analyses, as demonstrated in Fig. 26. Fig. 26 shows the sway

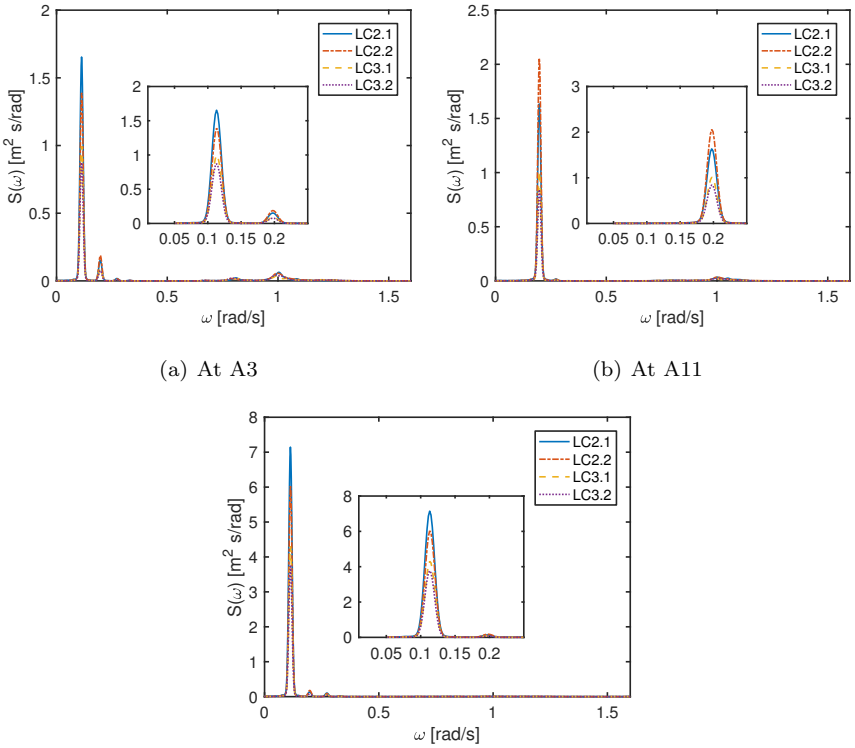

(a) At A3

(b) At A11

(c) At A16

Figure 26: Spectra of sway motion of girder nodes at (a) A11, (b) A16 under 100-year wave condition in LC3.

spectra in three representative locations, i.e. A3, A11, and A16. The standard deviation of sway is also dominated by low frequency resonant responses excited by second order difference-frequency wave forces. In the middle part (A11) the second mode is excited, while at two sides (A3 and A16), mainly the first mode is excited. Additionally, assessing the distribution of significant wave height along the bridge in LC3 indicates that significant wave heights at two sides are assumed to be 1.6 m and 2 m, respectively, which will of course give smaller wave-induced responses.

The standard deviation of heave motion in LC3 is shown in Fig. 27. For the south part of the bridge, the standard deviation of heave motion in LC3 is still

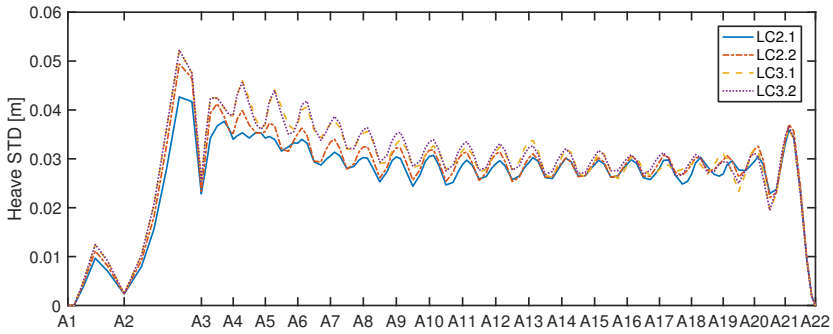

Figure 27: The standard deviation of heave motion along the bridge girder under 100-year wave condition in LC3.

larger than those in LC2.1. However, the differences between inhomogeneous waves (LC3) and homogeneous waves (LC2.1) actually decrease as compared to those shown in Fig. 18(b) between inhomogeneous waves (LC2.3 and LC2.4) and homogeneous waves (LC2.1). This is also due to reduction of significant wave height in LC3. Similar trends are also observed in the standard deviation of axial force, strong axis bending moment and weak axis bending moment, as shown in Fig. 28.

In general, the inhomogeneity in LC3 is achieved by decreasing the significant wave height at certain locations of the floating bridge, while the change in wave direction is not notable for each pontoon. Consequently, the wave induced responses are reduced due to smaller wave loads.

6. Concluding remarks

The wave load effect of an end-anchored curved floating bridge is investigated considering inhomogeneous wave conditions in this study. The coupled time domain code SIMO-RIFLEX is used to model and analyze the dynamic responses of the floating bridge.

An approach is proposed in this study to account for the inhomogeneous wave load effects. The wave excitation forces acting on each body are pregenerated given the wave spectra and body locations. Inhomogeneous wave conditions are

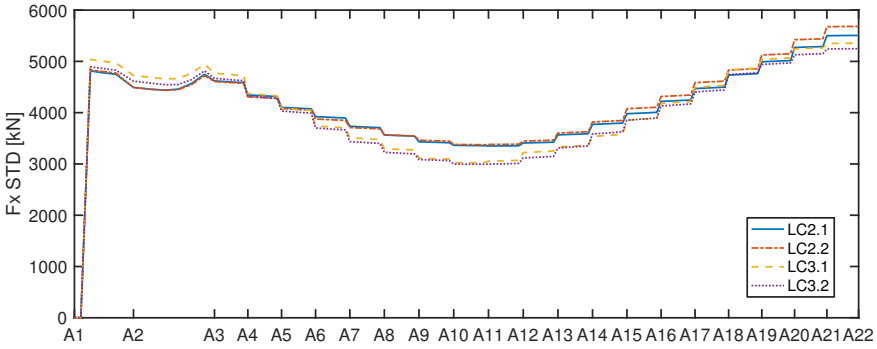

(a) Axial force, F_x

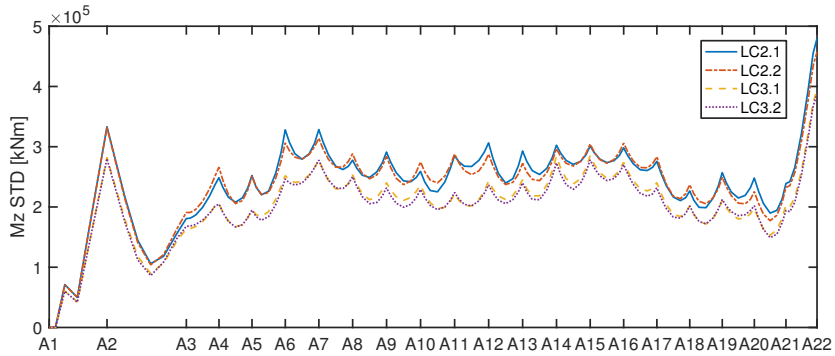

(b) Strong axis bending moment, M_z

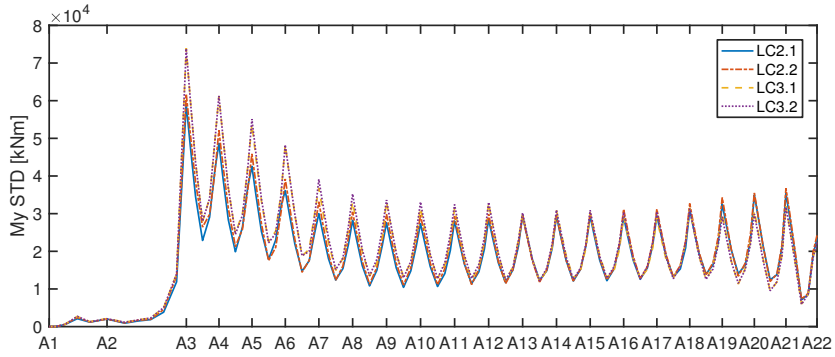

(c) Weak axis bending moment, M_y

Figure 28: The standard deviation of (a) axial force F_x, (b) strong axis bending moment, M_z, and (c) weak axis bending moment, M_y, along the bridge girder under 100-year wave condition LC3.

achieved by properly specifying wave spectra.

One 1-year (LC1) and two 100-year (LC2 and LC3) wave conditions are considered in this study. LC1 and LC2 have a fairly weak inhomogeneity, while LC3 has a stronger inhomogeneity. Dynamic responses considering inhomogeneous waves are compared with those considering homogeneous waves. It is found that weakly inhomogeneous waves (in LC1 and LC2) tend to cause relatively larger sway motion, axial force, and strong axis bending moment, and cause significantly larger weak axis bending moment. However, a stronger inhomogeneity (in LC3) causes smaller dynamic responses, due to smaller significant wave heights assumed for pontoons at two ends of the bridge. The difference with respect to random phase angle only does not give a significant effect on the responses; while the spatial variations of H_s, θ_p (and maybe T_p) give more influence on the responses. Proper description of inhomogeneous wave condition is thus of crucial importance when evaluating and considering the effect of inhomogeneous waves.

In summary, this study presents an approach to account for inhomogeneous wave load conditions on a floating bridge and investigates the inhomogeneous wave load effects of an end-anchored floating bridge. The effect of inhomogeneity is found to differ for various response variables. Therefore, the effect of inhomogeneous waves should be assessed based on a proper description of the wave field in a fjord. Measurements are needed to assess the wave conditions in fjords where floating bridges are to be used. Finally, the uncertainty in the response due to that in wave data and analysis methodology should be properly accounted for either by modifying load factors or using conservative data and models.

Acknowledgment

This work was supported by the Norwegian Public Roads Administration and in parts by the Research Council of Norway through the Centre for Ships and Ocean Structures (CeSOS) and Centre for Autonomous Marine Operations and

Systems (AMOS), at the Department of Marine Technology, NTNU, Trondheim, Norway. The support is gratefully acknowledged by the authors.

References

[1] Watanabe E. Floating bridges: past and present. Structural Engineering International 2003;13(2):128–32.

[2] Kvåle KA. Dynamic behaviour of floating bridges exposed to wave excitation: A numerical and experimental investigation. PhD thesis; Norwegian University of Science and Technology; 2017.

[3] Hartz B. Dynamic response of the hood-canal floating bridge. In: Second ASCE/EMD Specialty conference on dynamic response of structures. Atlanta, GA, USA; 1981,.

[4] Kvåle KA, Sigbjörnsson R, Øiseth O. Modelling the stochastic dynamic behaviour of a pontoon bridge: a case study. Computers & Structures 2016;165:123–35.

[5] Kvåle KA, Øiseth O, Rønnquist A. Operational modal analysis of an end-supported pontoon bridge. Engineering Structures 2017;148:410–23.

[6] Langen I, Sigbjörnsson R. On stochastic dynamics of floating bridges. Engineering structures 1980;2(4):209–16.

[7] Watanabe E, Maruyama T, Ueda S, Tanaka H. Yumemai Floating Swing Arch Bridge of Osaka, Japan. In: Large Floating Structures. Springer; 2015, p. 61–90.

[8] Løken AE, Oftedal RA, Aarsnes JV. Aspects of hydrodynamic loading and responses in design of floating bridges. In: Second symposium on strait crossings. Trondheim, Norway; 1990,.

[9] Raftoyiannis IG, Avraam TP, Michaltsos GT. Analytical models of floating bridges under moving loads. Engineering Structures 2014;68:144–54.

[10] Petersen ØW, Øiseth O. Sensitivity-based finite element model updating of a pontoon bridge. Engineering Structures 2017;150:573–84.

[11] Giske FIG, Leira BJ, Øiseth O. Long-term stochastic extreme response analysis of floating bridges. Procedia Engineering 2017;199:1175–80.

[12] Junyent EB, Biondini F, Titi A. Nonlinear structural analysis of floating bridges. In: Maintenance, Monitoring, Safety, Risk and Resilience of Bridges and Bridge Networks. CRC Press; 2016, p. 391.

[13] Xu Y, Øiseth O, Moan T. Time domain modelling of frequency dependent wind and wave forces on a three-span suspension bridge with two floating pylons using state space models. In: ASME 2017 36th International Conference on Ocean, Offshore and Arctic Engineering. American Society of Mechanical Engineers; 2017, p. V009T12A022.

[14] Sha Y, Amdahl J. Ship collision analysis of a floating bridge in ferry-free e39 project. In: ASME 2017 36th International Conference on Ocean, Offshore and Arctic Engineering. American Society of Mechanical Engineers; 2017, p. V009T12A021.

[15] Cheng Z, Gao Z, Moan T. Hydrodynamic load modeling and analysis of a floating bridge in homogeneous wave conditions. Marine Structures (submitted) 2017;.

[16] COWI . NOT-HYDA-018 Curved bridge navigation channel in south - environmental loading analysis. Report for the Norwegian Public Road Administration. COWI AS, Oslo, Norway; 2016.

[17] Cheng Z, Svangstu E, Gao Z, Moan T. Field measurements of inhomogeneous wave conditions in Bjørnafjorden. Submitted for journal publication 2017;.

[18] Wei W, Fu S, Moan T, Lu Z, Deng S. A discrete-modules-based frequency domain hydroelasticity method for floating structures in inhomogeneous sea conditions. Journal of Fluids and Structures 2017;74:321–39.

[19] Wei W, Fu S, Moan T, Song C, Ren T. A time-domain method for hydroelasticity of very large floating structures in inhomogeneous sea conditions. Marine Structures 2018;57:180–92.

[20] Wu Y, Ding J, Li Z, Ni X, Wu X, Tian C. Hydroelastic responses of vlfs deployed near islands and reefs. In: ASME 2017 36th International Conference on Ocean, Offshore and Arctic Engineering. American Society of Mechanical Engineers; 2017, p. V009T12A014.

[21] MARINTEK . Rifelx theory manual, version 4.0. 2012.

[22] MARINTEK . Simo-theory manual version 4.0. 2012.

[23] COWI . NOT-KTEKA-021 Curve bridge navigation channel in south summary of analyses. Report for the Norwegian Public Road Administration. COWI AS, Oslo, Norway; 2016.

[24] Lothe A, Musch O. Bjørnafjorden submerged floating tube bridge: sea state simulations. Tech. Rep.; Norconsult AS; 2015.

[25] SVV . Design basis metocean. Statens vegnesen, Norway; 2016.

[26] DNV GL . Environmental conditions and environmental loads (DNV-RP-C205). Det Norske Veritas AS, Oslo, Norway; 2014.

[27] Cummins WE. The impulse response function and ship motions. Institut fur Schiffbau, Universitat Hamburg, Hamburg; 1962.